High-harmonic spectroscopy of strongly bound excitons in solids

Simon Vendelbo Bylling Jensen [1,*] Lars Bojer Madsen [1] Angel Rubio [2,3,†] and Nicolas Tancogne-Dejean [2,‡]

[1]*Department of Physics and Astronomy, Aarhus University, DK-8000 Aarhus C, Denmark*

[2]*Max Planck Institute for the Structure and Dynamics of Matter and Center for Free-Electron Laser Science, Hamburg 22761, Germany*

[3]*Center for Computational Quantum Physics (CCQ), The Flatiron Institute, New York, New York 10010, USA*

(Received 7 July 2023; revised 22 March 2024; accepted 8 May 2024; published 4 June 2024)

We explore the nonlinear response of ultrafast strong-field-driven excitons in a one-dimensional solid with *ab initio* simulations. We demonstrate from our simulations and analytical model that a finite population of excitons imprints unique signatures to the high-harmonic spectra of materials. We show the exciton population can be retrieved from the spectra. We further demonstrate signatures of exciton recombination and that a shift of the exciton level is imprinted into the harmonic signal. The results open the door to high-harmonic spectroscopy of excitons in condensed-matter systems.

DOI: 10.1103/PhysRevA.109.063104

I. INTRODUCTION

When semiconductor or insulator systems interact with light, their optical linear and nonlinear responses are often dominated by features arising due to bound electron-hole pairs known as excitons [1]. Excitons are consequential in photonic technology [2] and play a significant role in many processes, such as energy transfer and light absorption in biomolecules [3,4], nanostructures [4], and solids [5,6], and have fundamental and technological applications. Bound excitons give rise to sharp peaks in absorption and photoluminescence spectra, which exhibit optical features such as the Stark effect [7], Rabi oscillations [8], and Fano resonances [9]. Understanding how they behave under external perturbations such as ultrafast intense fields is therefore key to making use of them for future applications like PHz electronics and guide experimental observations by providing microscopical understanding of their pump-probe data.

Excitons arise in different forms, such as interlayer excitons, optically dark excitons, strongly bound excitons, to name a few [6,10], and are important for the properties of bulk materials but also low-dimensional materials [11–14], van der Walls heterostructures [15], and twistronics [16,17]. The development of methods allowing to study the dynamics of excitons is an active area of research, including the study of exciton formation [18], ultrafast dynamics [19–21], condensation [22], dissociation [23], and coupling to other degrees of freedom [24,25].

While excitons are known to play important roles in many aspects of material science, and can even dominate in linear and perturbative nonlinear spectroscopies in solids, it is common to neglect excitonic effects in describing electron dynamics induced by intense laser fields. This approach is in the spirit of the strong-field approximation of atomic physics, in which the laser field is assumed to dominate over the Coulomb interaction [26], thus motivating a description in terms of independent particles. It is thus rationalized that either excitons do not form or that any bound exciton present in the material would dissociate during strong-field processes [27]. In this work, however, we show that for typical laser parameters used for strong-field physics in solids, this argument fails for strongly bound excitons. Indeed, the latter are shown to modify the ultrafast optical response of condensed-matter systems.

With recent experiments on exciton-mediated second-harmonic generation [28], nonlinear exciton dynamics in THz harmonic sideband generation [29–31], in attosecond transient reflection and absorption spectroscopy [32–35], it is crucial to elucidate the dynamics of excitons under intense laser fields, in order to support a complete understanding of light-matter interactions. Here we consider their impact on the process of high-order-harmonic generation (HHG). HHG utilizes the ultrafast nonlinear response of a material to generate ultrashort coherent pulses, which inherit spectrographic information from the underlying electron dynamics [36–44]. So far, most condensed-matter HHG experiments are rationalized in terms of independent-electron models, which ignore excitons, but are capable of describing energy-cutoff scaling, spectral features [42,45–48], orientation and polarization dependencies [49,50], as well as reconstruction of band structure [51,52] and Berry curvature [53] even if topological signatures in HHG remain elusive [54]. Experimental indications of possible excitonic effects have arisen in HHG as a plateau in rare-gas solids [55], an increased efficiency of monolayer compared to bulk crystals [56], and a characteristic delay dependency in pump-probe HHG [48]. However, a clear demonstration of excitonic effects related to a controlled exciton population in HHG remains elusive. In the semiconductor Bloch equations (SBE) formalism, it was already indicated that excitons could be important for interpreting the HHG mechanisms, as the relative importance of

*simon.jensen@mpsd.mpg.de
†angel.rubio@mpsd.mpg.de
‡nicolas.tancogne-dejean@mpsd.mpg.de

interband or intraband contributions are altered if the Coulomb interaction is tuned to reproduce accurate exciton binding energies [57]. Further, an enhancement of specific spectral HHG features is predicted if including the excitonic Coulomb interactions [58–60] and attributed to be a contributor in experiments [61]. Recently, excitons have also been predicted to influence HHG in Mott insulators and monolayer transition metal dichalcogenides, in the framework of effective Hamiltonian models [62–64]. Here, however, we do not examine systems with different degree of Coulomb interactions, a control knob which is not accessible in any experiment. Instead, we investigate the role of an exciton population in a practical pump-probe scheme. We note at last that exciton influence on HHG could be expected to share characteristics with HHG from excited states, two-level systems, or from dopant states in semiconductors [65–67].

II. THEORETICAL MODEL AND METHODS

A few approaches may capture excitons in real-time *ab initio* simulations, like nonequilibrium Green's functions (NEGF) [68–70], based on the generalized Kadanoff-Baym ansatz [71]. While important progresses have been made [21,72], this method is still numerically prohibitive, and one often needs to employ simpler methods like time-dependent Hartree-Fock (TDHF) [73], or the related hybrid functionals in time-dependent density-functional theory (TDDFT) [74] to be able to describe realistic materials or to scan over a wide range of laser parameters and excitation conditions. Hybrid functionals allow to explore ultrafast and nonlinear electrons dynamics [75] with low-cost and accurate alternatives to NEGF [76] but are restricted on, e.g., the dimensionality. Furthermore, the formalism within TDDFT to provide access to time-resolved visualization of the exciton wave function [77] can thus provide insights on the exciton dynamics in space and time and is also applicable for the more established TDHF formalism.

In light of this, we perform real-time *ab initio* wave-function-based TDHF simulations to characterize nonlinear ultrafast exciton dynamics and investigate how excitons modify the HHG response in a realistic pump-probe setting. Simulations are performed for a one-dimensional insulating hydrogen crystal that has strongly bound excitons [75,78], and is therefore ideal for unraveling the fundamental ultrafast exciton dynamics. Electrons are driven along the laser polarization direction through a periodic chain of hydrogen dimers with a bond length of 1.6 bohrs and lattice constant of $a = 3.6$ bohrs. The interaction between nuclei, located at x_i, and electrons is described with the softened Coulomb potential $v_{\text{ion}}(x) = -\sum_i [(x - x_i)^2 + 1]^{-1/2}$. The dynamics is solved by propagating a set of orthonormal electron orbitals $\varphi_i^{\text{HF}}(x, t)$, through the velocity gauge formalism of the TDHF equation and given in atomic units as

$$i\partial_t \varphi_i^{\text{HF}}(t) = \left\{ \tfrac{1}{2}[-i\partial_x + A(t)]^2 + v_{\text{ion}}(x) + v_H[n](x,t) + \widehat{v}_X\left[\left\{\varphi_j^{\text{HF}}(t)\right\}\right] \right\} \varphi_i^{\text{HF}}(t).$$

Here $A(t)$ is the vector potential describing the applied laser pulse in the electric dipole approximation. The electron-electron interaction is described by the Hartree potential $v_H[n](x,t) = \int dx' n(x',t)[(x-x')^2 + 1]^{-1/2}$, and the nonlocal exchange operator, which applied to an orbital is given as

$$\widehat{v}_X\left[\left\{\varphi_j^{\text{HF}}(t)\right\}\right]\varphi_i^{\text{HF}}(t) = -\sum_{k=1}^{N} \varphi_k^{\text{HF}}(x,t) \int dx' \frac{\varphi_k^{\text{HF}*}(x',t)\varphi_i^{\text{HF}}(x',t)}{[(x-x')^2+1]^{1/2}}.$$

The density is $n(x,t) = \sum_{i=1}^{N} |\varphi_i^{\text{HF}}(x,t)|^2$. The ground-state orbitals are obtained by a self-consistent iterative process of solving the HF equation starting from a linear combination of atomic orbitals using the OCTOPUS software package [79]. Hereafter, the TDHF equation is propagated using an enforced time-reversal symmetry propagator utilizing the adaptively compressed exchange operator formulation [80], and using a predictor-corrector scheme to guarantee that we reach self-consistency at every time step Δt, with $\Delta t = 0.242$ as. Furthermore, we apply a singularity correction to treat divergent terms from the exchange energy [81], that we adapted to the one-dimensional case.

The periodic hydrogen chain model calculation is performed using a converged real-space grid spacing of 0.4 bohrs. For the crystal momentum-space grid, convergence was achieved using 1024 grid points or increasing to 2048 grid points for the highly excited systems. Part of the band structure of the system is given in Fig. 1. From the band structure, we observe a direct band gap of 9.45 eV, which corresponds to 15.24 harmonic orders of the HHG-generating probe pulse with a wavelength of 2000 nm (∼0.62 eV).

The linear absorption spectrum is obtained by the application of a perturbative δ kick [82] followed by a time evolution, and is shown in Fig. 2. With this, we obtain the pump frequencies for exciting the system. The first one, $\omega_{\text{ex}} = 3.86$ eV, corresponds to resonantly driving the transition to the strongly bound exciton. The second one, $\omega_{\text{bg}} = 9.45$ eV, is resonant with the minimum band gap, where valence and conduction bands have a high density of states. This second transition can provide energy for an exciton-resonant transition from

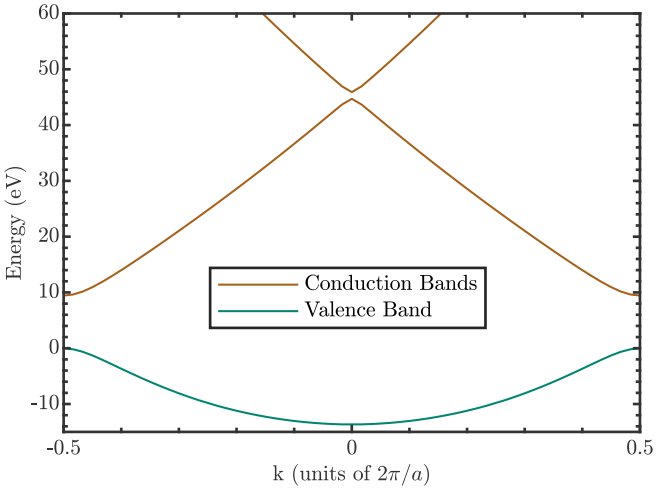

FIG. 1. Part of the band structure with the valence band and lowest-energy conduction bands. The band gap is found to be 9.45 eV.

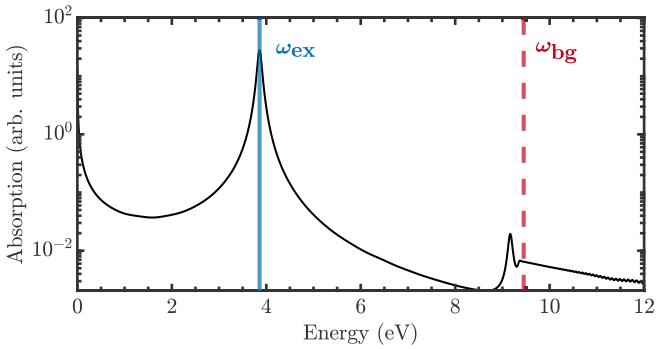

FIG. 2. Linear absorption spectrum calculated through TDHF with exponential dampening of the electronic current, corresponding to a Lorentzian broadening of the absorption spectrum. The vertical lines denote the two applied pump frequencies, the exciton-resonant one, at $\omega_{ex} = 3.86$ eV, and the band-gap-resonant one, at $\omega_{bg} = 9.45$ eV. We associate the peak just below the band-gap energy to be a signature of excited excitonic states.

lower-energy electrons of the valence band, however, with a weak coupling due to the low density of states at the associated section of the valence band.

Throughout our work a $\sin^2$-pulse shape is applied for both pump and probe pulses. The duration of the pump (probe) pulse is 25 fs (100 fs) with a peak-to-peak delay of 72.5 fs. The probe intensity is kept at 10^{12} W cm^{-2}, whereas a wide scan of pump intensities has been explored. For the pump-probe systems, we consider an experiment of orthogonally oriented polarization for the pump and probe pulse, respectively, such that the perturbative response of the pump is not present in the HHG spectra. To account for this along the one-dimensional model, we only consider the probe-induced current for the spectra, which is the current induced by the probe when affecting a pump-prepared system. Numerically this corresponds to considering $J(t) = J_{\text{pump-probe}}(t) - J_{\text{pump}}(t)$, with $J_{\text{pump-probe}}(t)$ being the system response to a pump-probe scheme, and $J_{\text{pump}}(t)$ being the system response to only a pump pulse. Here $J(t)$ is the electric current, evaluated by

$$J(t) = \sum_{i,\sigma} \int dx \, \text{Re}\left[\varphi^{\text{HF}*}_{i,\sigma}(x,t) \times \left(-i\frac{\partial}{\partial x} + A(t)\right)\varphi^{\text{HF}}_{i,\sigma}(x,t)\right].$$

From this, the HHG spectra are obtained as

$$S(\omega) = \left|\omega \int dt\, J(t) e^{-i\omega t}\right|^2. \tag{1}$$

When performing the Fourier transform, a window function is applied with a $\cos^8$ decay to attenuate the current at the very end of the simulated interval to avoid numerical artifacts.

A. Time-resolved exciton wave functions

Central to our work is the investigation of the exciton dynamics under intense laser interaction. For this reason, one needs to investigate exciton properties and hence needs to construct the exciton wave function. In our work, the exciton wave function is constructed from the single-particle transition density matrix (TDM), by the procedure of Ref. [77]. The protocol relies on the transition density matrix, which has been helpful for the analysis and interpretation of excited states of molecular systems. In quantum chemistry, the time-dependent TDM has been shown to be analogous to the exciton wave function given from Green's function theory [83]. When extended beyond the linear response regime for TDDFT and TDHF, the time-dependent TDM is constructed as a sum of weighted transition amplitudes. What makes it particularly useful is that the TDM offers a way to resolve a given excitation in a spatial map constructed of pure single-particle excitations. In that way, the time-dependent TDM, $\Gamma_s(x, x', t)$, for a given excitation represents weighted transition amplitudes of processes where a particle is annihilated at position x and created at position x' [84]. One can thus think of the TDM as accounting for the conditional probability of finding an electron at a certain place given the position of the associated hole. For real-time TDHF, the time-dependent TDM can be calculated at a specific time t utilizing the HF orbitals at that time $\varphi^{\text{HF}}_{\sigma,i}(x,t)$, which have been propagated from their ground state $\varphi^{\text{HF}}_{\sigma,i}(x,t=0) = \varphi^{\text{HF}}_{\sigma,i}(x)$. The time-dependent TDM is denoted here as the difference between the time-dependent and the ground-state one-body density matrices, which can be evaluated as

$$\Gamma_s(x,x',t) = \sum_{i}^{\text{occ}} \left[\varphi^{\text{HF}}_i(x,t)\varphi^{\text{HF}*}_i(x',t) - \varphi^{\text{HF}}_i(x)\varphi^{\text{HF}*}_i(x')\right]. \tag{2}$$

For periodic systems, it is expressed using the knowledge of orbitals inside the unit cell thanks to Bloch's theorem. However, the distances x and x' of the time-dependent TDM reside in the full crystal, given by the unit-cell volume multiplied by the number of k points used in the simulation. Indeed, the exciton occupies the entire crystal structure. To associate some physical insight into the TDM, we note that the diagonal of the TDM contains the time-dependent density response associated with the given excitation $\Gamma_s(x,x,t) = \delta n(x,t)$, with $\delta n(x,t) = n(x,t) - n(x,t=0)$. Since the integrated density remains constant with time, this enforces that $\int dx[\Gamma_s(x,x,t)] = 0$. In obtaining the time-dependent TDM in real space, one can extract information with regards to the dynamical exciton processes, such as dissociation rates or charge separation rates. A complete quantitative analysis would require to scan both the electron and hole coordinates. But due to the large-scale structure of the TDM being diagonally dominated, we conclude that qualitative features can be inferred from the TDM with the hole placed at the center between the two nuclei. In the following, we refer to $\Gamma_s(x, x'=0, t)$ as the exciton wave function for the case of the hole being localized at $x' = 0$.

In the reference frame of the hole, the first moment of the exciton wave function is given as [85,86]

$$m = \int dx|x||\Gamma_s(x,0,t)|^2 \Big/ \int dx|\Gamma_s(x,0,t)|^2, \tag{3}$$

and normalized to the excitation magnitude. The first moment of the exciton wave function reveals the degree of localization

of an excitation (in this case around $x' = 0$), and can therefore in principle allow us to distinguish between bound excitons and free carriers. Indeed, if the material contains strongly bound excitons, m is of a few Å since the electron is very likely to remain near its hole. Inversely, if a material contains free carriers and conduction bands are dispersive, then electrons are delocalized throughout the crystal, and m increases to the size of the crystal, which for our case is hundreds of Å. Note that m is used to define the exciton radius from *ab initio* simulations [87]. The exciton wave function can be further analyzed utilizing the first moment to distinguish the relative population of excitons and free carriers as outlined in Appendix A.

III. RESULTS AND DISCUSSION

A. Ultrafast exciton processes for HHG

1. Exciton preparation

We first investigate how an exciton population in the material can be created. For this, we pump the material with a laser under different excitation conditions. We need to define a criterion to isolate the effect of the pump laser regarding excitation of free carriers or excitons. We determine the nature of the excitation by analyzing the real-time dynamics of the exciton wave function $\Gamma_s(x, x', t)$ of Eq. (2) and its first moment as provided by Eq. (3).

Figure 3(a) reveals that while for band-gap resonant pumping we only generate free carriers with a large first moment m, for exciton resonant pumping m attains smaller values suggesting appreciable population of excitons, as is expected for the exciton-resonant pumping [68]. At low intensity, indicated by the blue area, we generate mostly bound excitons, as also shown by the exciton density of Fig. 3(c). For high intensity, indicated by the red area, the population of free carriers clearly dominates the excitation. This is also visible from the exciton density of Figs. 3(d) and 3(e). We use m to differentiate the nature of the excitation and extract the number of free carriers N_{fc} of Eq. (A1) and the number of excitons N_{ex} of Eq. (A3) as outlined in Appendix A. These are provided for the various excited systems in Fig. 3(f). We observe that the generation of excitons by the ω_{ex} pump deviates from the first-order perturbative response, indicated by the dashed blue line. This deviation can be attributed to a subsequent exciton dissociation process occurring during the pumping, as the pump ionizes the excitons it creates. Alternative mechanisms, such as nonlinear effects associated with three-photon excitations directly to the band gap, are excluded as this would reflect in a change of the slope of the power law in Fig. 3(f). On the contrary, the ω_{bg}-pumped systems prepare dominantly free carriers at all intensities and follow the perturbative scaling. We note that the difference in the excitation magnitudes for the two pump frequencies in Figs. 3(c)–3(f) can be rationalized from the relative resonance magnitudes in the linear absorption spectra of Fig. 2.

To further elucidate the exciton dissociation process by the intense pump pulses we now perform simulations of the exciton dynamics under the envelope approximation, as described in detail in Appendix B. For this, we let the exciton wave packet evolve in time under the influence of the pump laser

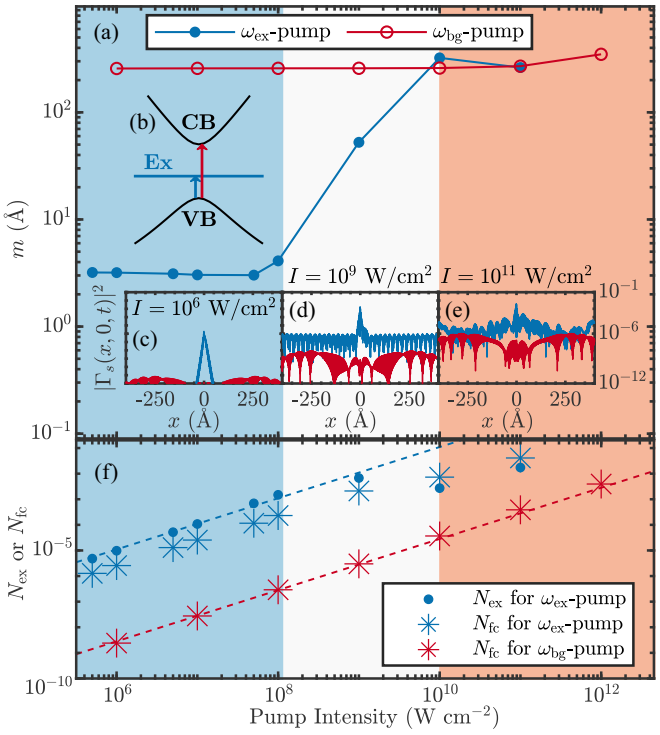

FIG. 3. (a) First moment, m of Eq. (3), of the approximated exciton wave function for different pump frequencies and intensities. The areas denote regimes where the ω_{ex} pump generates dominantly bound excitons (blue) or free carriers (red). (b) Excitation pathways from the valence band (VB) to conduction band (CB) or to exciton (Ex). The corresponding energies are $\omega_{\mathrm{bg}} = 9.45$ eV and $\omega_{\mathrm{ex}} = 3.86$ eV. [(c)–(e)] Exciton density for a hole at $x' = 0$, after excitation by a 25-fs pump pulse with intensities of 10^6, 10^9, and 10^{11} W cm^{-2}, respectively. (f) Number of pumped free carriers N_{fc} and excitons N_{ex} in the system as of Eqs. (A1) and (A3). The dashed lines show the linear perturbative scaling behavior for resonant excitation. The highest intensity value for the ω_{ex} pump is omitted due to the excitation exceeding the damage threshold predicted under the electron-hole plasma model of ≈10% of excited electrons [88–90]. The quantities of [(a)–(f)] are evaluated after the pump preparation, just before the system is driven to produce HHG.

and we place absorbing boundaries at a distance of 500 bohrs from the center of the simulation box, to absorb the part of the wave packet that dissociates under the influence of the laser. This allows us to estimate the fraction of dissociated exciton population for various laser intensities. The results of the simulations are shown in Fig. 4. This simple modeling shows that pump-induced exciton dissociation is a very important when the intensity reaches values closes to 10^{11} W cm^{-2} and above. In a pump-probe setting, the pump intensity for the exciton transition therefore needs to be selected with care, to not dissociate the excitons with the pump itself.

2. Signatures of exciton dissociation for HHG

We now investigate the effect of a finite-exciton population on the HHG process by performing simulations where the material is excited by an exciton-resonant pump compared to the unpumped material. Differences between the considered cases (unpumped, band-gap-resonant pumping, and

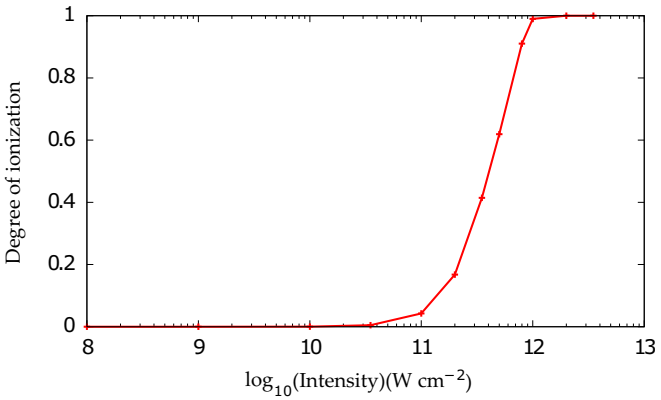

FIG. 4. Degree of ionization of the exciton induced by a pump laser versus different intensities utilizing identical laser parameters as for Fig. 3 in the main text. See main text for details.

exciton-resonant pumping) start to emerge when the pump excites more than 10^{-5} valence electrons per unit cell. Below such excitation degrees, only minor discrepancies around the pump frequencies are present in the pumped systems compared to the unpumped system spectra, which exhibit similar features as those of Ref. [78].

To investigate the signatures of exciton dynamics in HHG, in Fig. 5 we perform a time-frequency analysis of the harmonic emission comparing the exciton-resonant pump case to the unpumped case. Above the band gap, the time-frequency analysis reveals that the exciton-seeded system is starting to emit harmonics prior to the unpumped sample. The earlier nonlinear response time can be attributed to the dissociation of excitons requiring a weaker field strength than the excitation of electrons through the band gap. The two-step process in which an exciton is generated and afterwards dissociated could thus play a dominant role. The dissociation dynamics are directly observed if considering the evolution of the exciton wave function in Fig. 6. The initial emission time, at 75 fs in Fig. 5(a), corresponds to the time where substantial exciton dissociation is observed for the exciton wave

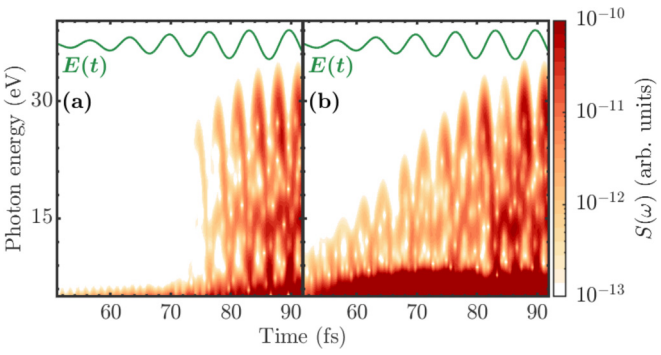

FIG. 5. Time-frequency analysis of the harmonic radiation of the region above the exciton binding energy for, respectively, an unpumped (a) and an exciton-seeded sample (b), obtained by an exciton-resonant pump with an intensity of 10^7 W cm^{-2}. The 2000-nm driving electric field is sketched in green and the time-frequency analysis is performed with a Gabor transform window of $\sigma = 0.40$ fs.

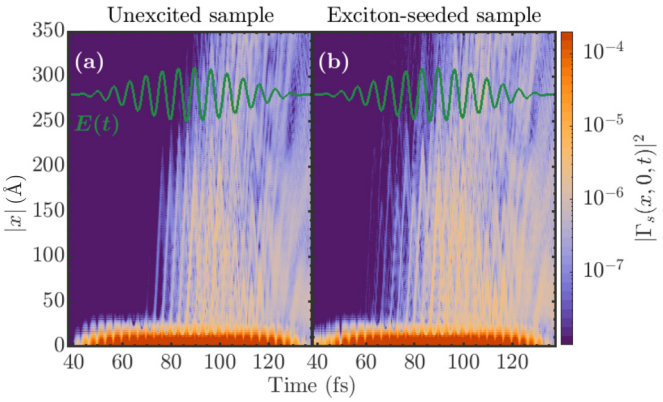

FIG. 6. Norm-squared exciton wave function as a function of distance and time, during the HHG process. Comparing an (a) unpumped system with (b) an exciton-seeded system with parameters of Fig. 5. The exciton wave function is considered within the temporal region of the probe pulse, which electric field is inserted in green.

function of Fig. 6(a), indicating that ionization of excitons is primarily responsible for the early stage of the harmonic emission. For the exciton-seeded sample in Fig. 6(b) the exciton wave function dissociates earlier to produce carriers within the first conduction band and contribute to the interband transitions of Fig. 5(b).

Based on our results, we note that pumping excitons in the sample look favorable with regard to decreasing the nonlinear response time of a condensed-matter system compared to an unpumped system. Similarly, pumping excitons in the sample also look favorable for enhancing interband harmonic emission, as is considered in Appendix C.

3. Signatures of exciton recombination for HHG

Commonly, the time-frequency analysis of the harmonic emission in solids reveals two contributions: a chirped emission related to the interband emission channel, and a chirpless emission due to the intraband motion of the electrons [91]. The standard approach to explain the chirped trajectories is to use a semiclassical interband model developed from a saddle-point approximation of the SBE [92]. The model has succeeded in describing cutoff energies, and extended to capture imperfect collisions and umklapp scattering [93,94]. Opposed to the typical setting, if magnifying the time-frequency analysis of Fig. 5 in Fig. 7, we observe not one set of chirped trajectories, but two, which calls for an exciton extended semiclassical model. We extend the model to include recombination paths associated with excitons, but note that imperfect collisions and umklapp scattering might also intricate the dynamics here. The first step of the interband model is the generation of a electron-hole pair at the band gap of the solid. We note that dissociation of excitons can also impact the ionization step of the semiclassical model. However, this leads to the same trajectories as the formation of free carriers when pumping electrons directly to the CBs. We therefore cannot distinguish signatures of exciton dissociation directly from the electron trajectories. The relative distance $\Delta x(t)$ between the generated electron and hole is now propagated from the generation time t_0 using the conduction and valence band

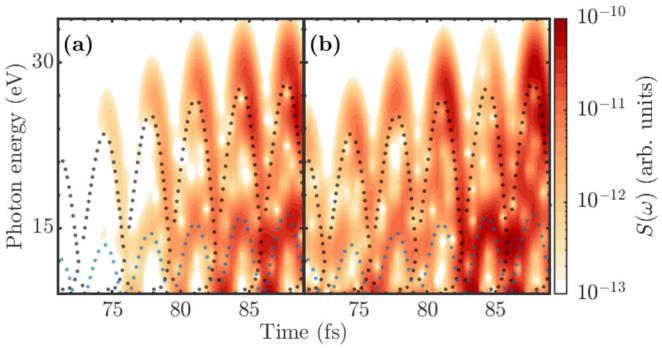

FIG. 7. Magnified time-frequency analysis of Figs. 5(a) and 5(b) for, respectively, an unpumped and exciton-seeded sample. Obtained with parameters of Fig. 5. Trajectories from our exciton-extended semiclassical model are depicted with dotted lines. Black color depicts trajectories recombining to the valence band and the blue color corresponds to recombination in form of a bound exciton.

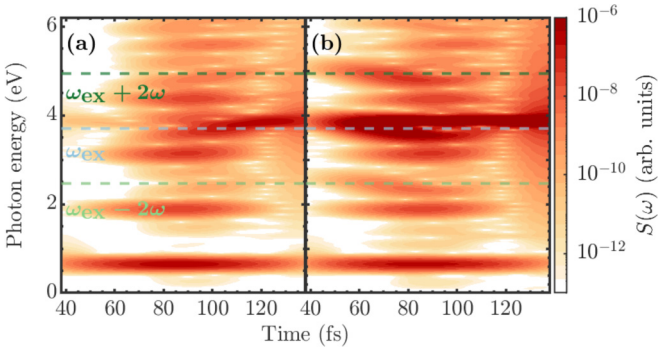

FIG. 8. Time-frequency analysis of the harmonic radiation in the spectral region below the band gap for, respectively, an (a) unpumped and an (b) exciton-seeded sample, obtained by an exciton-resonant pump similarly to Fig. 5. A window of $\sigma = 10$ fs is applied for the Gabor transform. Dashed lines denote the locations of the exciton peak, as well as the first exciton sidebands.

velocities $v_c(k)$ and $v_v(k)$ as

$$\Delta x(t) = \int_{t_0}^{t} \{v_c[k(t')] - v_v[k(t')]\} dt'. \tag{4}$$

The relative velocity is expressed from the curvature of the band structures for the valence and conduction bands, $\varepsilon_v(k)$ and $\varepsilon_c(k)$, as

$$v_c(k(t')) - v_v(k(t')) = \frac{\partial[\varepsilon_c(k(t')) - \varepsilon_v(k(t'))]}{\partial k}, \tag{5}$$

with crystal momenta governed by the acceleration theorem

$$k(t) = k_0 + A(t). \tag{6}$$

During propagation, the electron and hole might recombine at a recombination time t_r, where $\Delta x(t_r) = 0$, if neglecting imperfect recombinations as discussed in Refs. [93,95,96]. At the recombination step, the electron and hole pair is assumed to recombine and emit their excess energy.

This leads to an emission of light at the separation energy $\varepsilon_c[k(t_r)] - \varepsilon_v[k(t_r)]$, which grants the emission pattern shown by the black dots in Figs. 7(a) and 7(b). Here we extend the semiclassical model in order to explain the other set of trajectories. More precisely, we modify the recombination step to allow recombination into an exciton with binding energy E_b with emission of $\varepsilon_c[k(t_r)] - E_b$, similar to the recombination into a donor-doped state [67]. This leads to the emission pattern shown by the blue dots in Figs. 7(a) and 7(b). This recombination channel captures the second set of trajectories, thus revealing the importance of exciton recombination in the subcycle nonlinear electron dynamics. Since the energy goes into the formation of the exciton, the resulting harmonic emission energy is reduced, and the trajectories do not affect the high-energy part of the spectrum nor the energy cutoff. We note that similar subcycle features are observed to arise due to HHG from excited atomic states [65].

Apart from the new set of exciton-related trajectories, our simulations also reveal the appearance of exciton-related features in the below-band-gap energies, as shown in Figs. 8(a) and 8(b). For the unpumped system of Fig. 8(a), a continuous emission of clean odd-order harmonics is observed, as well as a resonance corresponding to the energy for generating or annihilating an exciton, as also observed in Ref. [78]. This is the expected subcycle dynamics for intraband emission [97]. For the exciton-seeded system of Fig. 8(b) we see that the exciton resonance is enhanced throughout and leads to continuous emission of weaker spectral features, corresponding to sidebands of the exciton resonance, located at $\omega_{ex} \pm 2\omega$. Such sidebands occur as a consequence of the prepared population of excitons being driven by the probe pulse to annihilate. In doing so, the partly dissociated excitons can undergo a laser-assisted electron-hole recollision process where photons can be exchanged with the strong electromagnetic field [29–31]. Opposed to these THz excitonic sideband experiments, here we predict sideband generation, where energies above 1 eV are exchanged with the electromagnetic field. For these quasiparticle collisions to occur, the sample needs a significant population of excitons.

4. Signatures of exciton energy shift

In the time-frequency analysis of Fig. 8, it is observed that the exciton features of the harmonic spectra are shifted in energy during the interaction with the driving pulse. This leads to, e.g., the exciton features of the harmonic spectrum having a wider spectral width, when considering the HHG spectra in the following Fig. 10. Such energy shift could be a result of a weakening of the binding energy due to presence of excited carriers, or mechanisms such as the excitonic Stark effect. We report the energy shift to be increasing with the intensity of the probe pulse, and thus the degree of excited carriers. To support this, we provide time-frequency analysis with a scan of probe intensities in the regime of 10^{11} to 2×10^{12} W cm^{-2} for the exciton-seeded sample of Fig. 8(b). A time-frequency analysis of the emitted harmonics during the probe pulse is given in Fig. 9, and we clearly observe how the exciton resonance and sidebands have a larger displacement in energy at higher pulse intensities.

B. HHG spectroscopy of strongly bound excitons

To utilize the spectroscopic capabilities of the harmonic exciton resonance and sidebands, we consider the harmonic

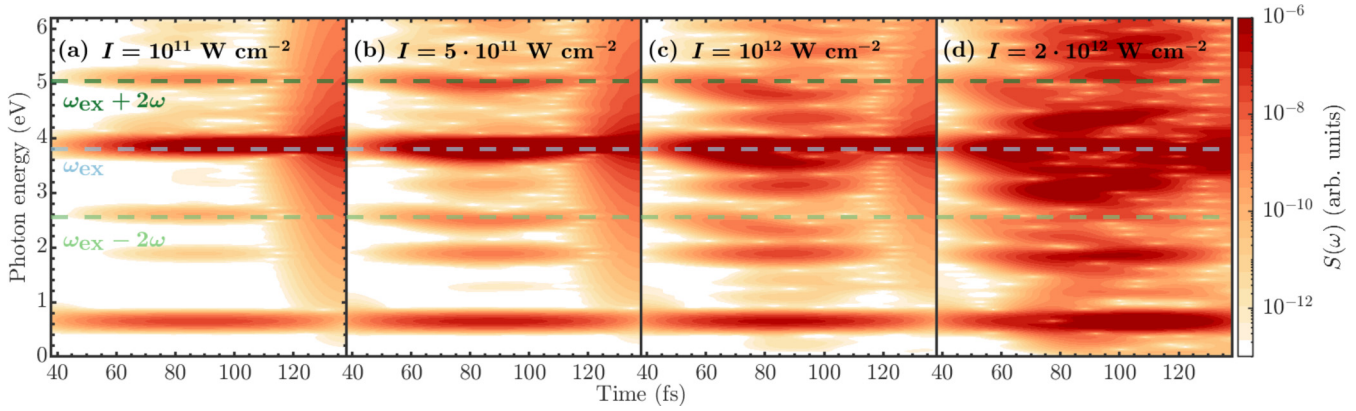

FIG. 9. Time-frequency analysis of the below-band-gap harmonic radiation for an exciton-seeded sample, obtained by an exciton-resonant pump with an intensity of 10^7 W cm^{-2}. The probe-pulse intensity is scanned in the regime of 10^{11} to 2×10^{12} W cm^{-1} and given in the caption. We used a window of $\sigma = 10$ fs for the Gabor transform. The positions of the exciton peak and the first exciton sidebands are denoted with dashed lines.

emission spectra in Figs. 10(a)–10(c) for a system driven with a 1600-, 2000-, or 2600-nm probe pulse. All our simulations showed exciton-induced sidebands, irrespective of probe duration and intensity. The signals from the unexcited system are given by the black curves and provide clean harmonic peaks with the inclusion of an exciton resonance at ω_{ex}. For the exciton-seeded system, prepared with a 10^7-W cm^{-2} pump pulse, the bound-exciton population contributes to an enhancement of the harmonic spectrum at the exciton energy, and its spectral sidebands in the regions marked with blue and green. This result shows that the sidebands can be observed over a range of laser wavelengths and are a robust feature of HHG from exciton-seeded materials. Using our simulated pump-probe setup, we now vary the exciton population by varying the pump intensity, and we track how the exciton resonance and sidebands are enhanced when increasing the exciton population. We find that the exciton peak and the sidebands follow the same power law $N_{ex}^{0.92}$ [see dashed lines in Fig. 10(d)], confirming their common origin. This scaling deviates from the expected linear scaling, indicating that other processes such as probe-induced exciton dissociation are taking place during the probe pulse. We note that at high degree of exciton preparation, $\pm 4\omega$ sidebands start to emerge in the HHG spectra but the associated enhancement is too low to be properly analyzed. Importantly, the direct relation between the population of bound excitons and the spectral weight of the exciton peak and sidebands opens the door to ultrafast all-optical method of probing of exciton population. We also note that longer wavelengths seem to produce more intense exciton peaks and sidebands. It is therefore interesting to employ longer wavelengths to probe excitonic signatures.

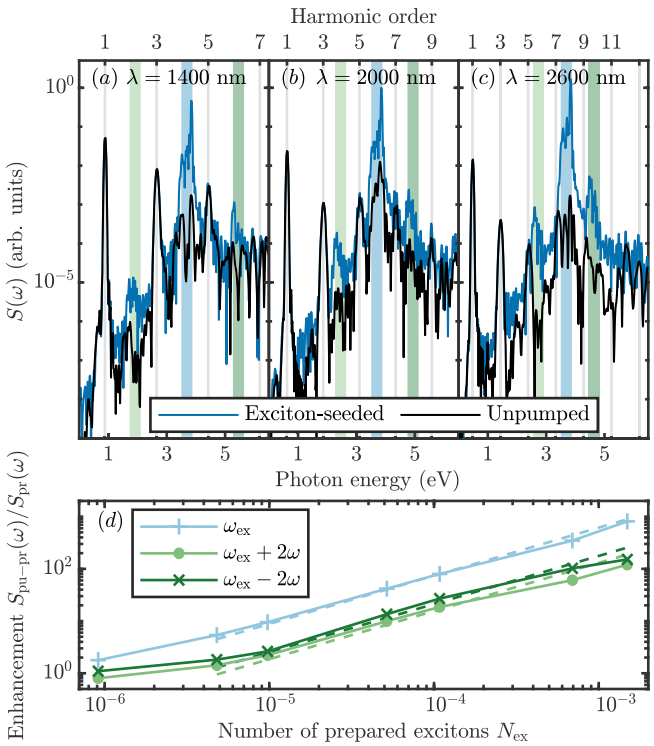

FIG. 10. [(a)–(c)] HHG spectra for various wavelengths for the unpumped system versus the system prepared by an exciton-resonant pump. The HHG driving probe wavelength is scanned across 1600, 2000, and 2600 nm, respectively, for [(a)–(c)]. The colored areas denote the exciton resonance (blue) and the first excitonic associated sidebands, at $\omega_{ex} \pm 2\omega$ (green). (d) Harmonic yield enhancement of the exciton resonance and sidebands for $\lambda = 2000$ nm as a function of bound exciton population, utilizing a 10^5–10^8 W cm^{-2} exciton-resonant pump. Dashed lines are explained in the main text.

IV. SUMMARY AND CONCLUSION

In summary, we investigated how a prepared population of strongly bound excitons affect HHG in a one-dimensional solid, by modeling a pump-probe setup, thus gaining insight into ultrafast exciton dynamics and revealing signatures of exciton dissociation and recombination. The behavior of exciton preparation under an intense pump was studied, revealing that the pump can dissociate the excitons it creates, leading to more free carriers than excitons when the pump reaches high intensities. The role of strong-field-driven excitons in HHG was further examined depicting intricate spectral features. The key spectral findings were found to be twofold: the presence of an exciton level allows for new excitation and recombination

pathways. To reveal this, we developed an exciton-extended semiclassical interband model, from which we could explain how the carriers recombine into bound excitons. In addition, we observed how the presence of a finite population of bound excitons is able to enhance the HHG process in the region of the excitonic resonance, in particular leading to excitonic sidebands whose intensity was found to be close to proportional to the exciton population. We finally proposed HHG spectroscopy as a viable method of extracting information both regarding finite population of strongly bound excitons as well as regarding their strong-field-driven dynamics. The emergence of sensitive on-chip techniques for PHz-scale optical-field sampling provides experimental possibilities to temporally unravel such ultrafast light-driven exciton dynamics [91]. There are still interesting questions to be addressed. While we have investigated strongly bound excitons, the role of continuum excitons as observed in semiconductors, carrier-induced screening, exciton-exciton interaction, and dimensionality remains to be explored.

ACKNOWLEDGMENTS

This work was supported by the Independent Research Fund Denmark (Grant No. 9040-00001B). S.V.B.J. further acknowledges support from the Danish Ministry of Higher Education and Science. Fruitful discussions with S. Latini are acknowledged. This work was supported by the Cluster of Excellence Advanced Imaging of Matter (AIM), Grupos Consolidados (IT1249-19), SFB925, "Light induced dynamics and control of correlated quantum systems." The Flatiron Institute is a division of the Simons Foundation.

APPENDIX A: NUMBER OF EXCITONS AND FREE CARRIERS

We want to extract information from the exciton wave function $\Gamma_s(x, x' = 0, t)$ to give a description of the number of excitons or free carriers in a given excitation. To do this, we consider the exciton wave function and assume that it consists of the contributions from excitons and free carriers. We assume that exciton population gives a localized exciton wave function or, in other words, a large conditional probability of finding the electron near its hole. As observed in Figs. 3(c) and 3(d), an exciton will attain a wave function with exponential scaling with distance and a first moment of less than 5 Å. The other contribution to the exciton wave function is originating from free carriers. We assume that these latter carriers provide a relatively uniform distribution of the exciton wave function with regards to distance. This is since the excited carriers are traversing freely throughout the lattice and thus have a uniform conditional probability for finding electron relative to its hole. Based on these two different contributions to the exciton wave function, we can interpret the ratio of such contributions to imply the ratio of excitons to free carriers for a given excitation. Normalizing these measures with the number of excited valence electrons per unit cell N_e, we can obtain the number of excitons N_{ex} and the number of free carriers N_{fc} for a given excitation.

The number of free carriers can be calculated as the contribution of the exciton wave function, which is uniform with respect to distance. To calculate this contribution, we integrate the exciton wave function from beyond the point at which the excitonic contribution is dominant, which we denote as the exciton radius r_{ex}. The average value of the exciton wave function in this region is then extended across the full crystal length L, being a times the number of momentum space grid points, to give the free-carrier contribution to the exciton wave function. The ratio of this contribution to the total size of the exciton wave function provides the ratio of free carriers for the excitation and multiplying with number of excited valence electrons, we obtain the number of free carriers as

$$N_{fc}(t) = N_e(t)\frac{L}{L - r_{ex}}\frac{\int_{r_{ex}}^{L} dx|\Gamma_s(x, 0, t)|^2}{\int_0^L dx|\Gamma_s(x, 0, t)|^2}. \tag{A1}$$

The radius of the bound exciton is in Fig. 3(a) identified to be $r_{ex} = 5$ Å for the model system in the low-exciton concentration regime. The number of excited valence electrons per unit cell is defined as

$$N_e(t) = N_{tot} - \sum_{n,n'}^{occ} \left|\langle\varphi_n^{HF}(t)|\varphi_{n'}^{HF}(t = 0)\rangle\right|^2, \tag{A2}$$

and is computed during our simulations, with N_{tot} being the total number of valence electrons. This allows us to compute $N_{fc}(t)$ from $N_e(t)$ and $\Gamma_s(x, 0, t)$. The remaining excitation must then consist of excitons, which can be found from

$$N_{ex}(t) = N_e(t) - N_{fc}(t). \tag{A3}$$

We note that with the definitions from Eqs. (A1)–(A3) a completely uniform exciton wave function will give $N_{fc} = N_e$ and $N_{ex} = 0$. Similarly the limit of completely localized electron wave function within r_{ex} will provide $N_{fc} = 0$ and $N_{ex} = N_e$.

It is interesting to compare our definition with prior works. In the context of semiconductor Bloch equations, a lot of effort has been devoted to define the coherent population of excitons. An extensive discussion can be found in the chapter "Coherent vs incoherent excitons" of Ref. [98]. In this chapter, one finds that the electron-hole pair correlation function [Eq. (27.27)] is nothing but the square modulus of the exciton wave function defined in our work. As explained in the book chapter, see in particular Eq. (27.29), this contains a "background contribution" [see in Eq. (27.30)]. While we do subtract this background, we do not do it as in the work of Koch and Kira, as we still have the contribution from the second term of their Eq. (27.31) included. Removing this contribution would require solving an extra equation, equivalent to their Eq. (27.34), and it is unclear what this equation would be in the context of TDHF. We therefore have defined a quantity which is free of the uncoherent background of free carriers, but this is not exactly the "true exciton population" defined by Koch and Kira [98].

APPENDIX B: EXCITON MODEL WITHIN THE EFFECTIVE MASS APPROXIMATION

To further understand the effect of the probe laser on the exciton population, we modeled the dynamics of the exciton within the effective mass approximation. For this we follow the works of Ogawa and Takagahara [99,100] that we

extend to the time-dependent case. Here we review the derivation starting from a three-dimensional two-body electron-hole time-dependent Schrödinger equation within a laser field linearly polarized along the z direction:

$$i\partial_t \Phi(\mathbf{r_e}, \mathbf{r_h}, t) = \Big(\frac{1}{2m_e}[-i\nabla_e + \mathbf{A}(t)]^2 + \frac{1}{2m_h}[-i\nabla_h - \mathbf{A}(t)]^2 + U_e(\mathbf{r_e}) + U_h(\mathbf{r_h}) + V(\mathbf{r_e}, \mathbf{r_h}) \Big) \Phi(\mathbf{r_e}, \mathbf{r_h}, t),$$

where $\Phi(\mathbf{r_e}, \mathbf{r_h})$ is commonly referred to as the exciton envelope function, m_e (m_h) is the effective mass of an electron (a hole), V is the Coulomb interaction, U_e (U_h) the confining potential acting on the electron (hole), and $\mathbf{A}(t) = A(t)\hat{\mathbf{e}}_\mathbf{z}$ is the vector potential of the laser.

Assuming a strong confinement of the carriers in the lateral directions, we can apply the envelope approximation, which assumes that [100]

$$\Phi(\mathbf{r_e}, \mathbf{r_h}, t) = e^{iKZ} f_e(x_e, y_e, t) f_h(x_h, y_h, t) \phi(\mathbf{r_e} - \mathbf{r_h}, t),$$

where Z and K are z coordinates of the center of mass of the exciton and the corresponding wave number, and f_e and f_h are the lowest subband functions in the lateral directions for the electron and the hole. Finally, ϕ describes the relative motion of the electron and the hole. After some algebra, and assuming that f_e and f_h remain normalized to unity at all times and that ϕ only depends on $z = z_e - z_h$, we obtain a one-dimensional time-dependent Schrödinger equation

$$i\partial_t \phi(z, t) = \Big\{ \frac{1}{2\mu}\big[\partial_z + A(t)\big]^2 + \frac{1}{2(m_e + m_h)} K^2 + V_{\text{eff}}(z) \Big\} \phi(z, t),$$

where μ is the exciton reduced mass, $V_{\text{eff}}(z) = \int dx_e dy_e dx_h dy_h V(\mathbf{r_e}, \mathbf{r_h}) |f_e(x_e, y_e)|^2 |f_h(x_e, y_e)|^2$ is the confinement potential. We used here the fact that the confining potentials U_e and U_h are time independent, and hence the V_{eff} is time independent. Assuming that the energy of the center-of-mass motion $\frac{1}{2(m_e+m_h)}K^2$ remains constant during the time evolution, this term can be transformed away, and we have thus reduced the exciton problem to time evolution of a one-dimensional problem of a single particle within an electric field, with the only change that the particle has a reduced mass μ. This equation is easily solved using any software capable of propagating in time a one-dimensional time-dependent Scrödinger equation and, in this work, this is numerically solved using the OCTOPUS code [79]. We employed here a grid spacing of 0.4 bohrs, and used a simulation for a radius 600 bohrs, including 100-bohrs-wide absorbing boundary region using a complex absorbing potential of height 0.2 a.u. with a sine-square envelope [101].

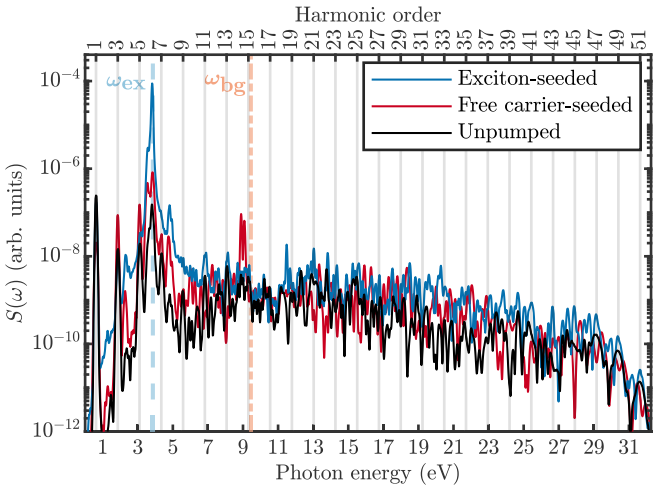

FIG. 11. High-harmonic generation spectra for the systems prepared with a large population of bound excitons with ω_{ex} or free carriers with ω_{bg}. The excited systems are prepared with a 10^8-W cm^{-2} ω_{ex} pump or a 10^{12}-W cm^{-2} ω_{bg} pump to generate a strong excitation of, respectively, bound excitons or free carriers. The total excitation prepared by the ω_{bg} pump is 2.3 times larger than the excitation generated by the ω_{ex} pump, as given in Fig. 1(f) of the main text. The harmonics is obtained when driven with a 2000-nm probe of intensity 10^{12} W cm^{-2}. The exciton resonance and the band-gap energy are marked with a blue dashed and red dashed-dotted line, respectively. For illustrative purposes, the spectra have been smoothed. See text in Sec. III for pulse durations and delay.

APPENDIX C: EXCITON-SEEDED INTERBAND ENHANCEMENT

In the strong excitation regime, we have investigated the spectral features arising from a large population of free carriers or excitons. To do this, we consider an exciton-seeded system prepared with a 10^8-W cm^{-2} ω_{ex} pump, which is known to produce a large population of bound excitons from Fig. 3(f). To compare, we choose a 10^{12}-W cm^{-2} ω_{bg} pump, as this generates an excitation, which is 2.3 times larger in magnitude than the ω_{ex} pump, but consists mainly of free carriers with a small fraction, 1%, of bound excitons. Here excitons can be generated both as a consequence of free-carrier recombination, or by the ω_{bg}-pump coupling directly to excited or ground exciton states from the valence band. Both systems are now prepared in a state with a large excitation and we thus observe a more convoluted system response in Fig. 11. Considering, e.g., the free-carrier-seeded system response, we see an enhancement of the exciton resonance and side peaks as well since this system is also seeded with a significant fraction of excitons. Actually, the number of excitons generated here is comparable with the exciton-seeded system of Fig. 10(b), which shows a similar enhancement of the exciton-related peaks. For the intense exciton-seeded spectrum in Fig. 11, we observe a more significant enhancement of the exciton peak and side peaks. Furthermore, we also observe the exciton-seeded sample to exhibit an enhancement across the first plateau. This enhancement can be attributed to a significant part of the seeded bound exciton population dissociating to

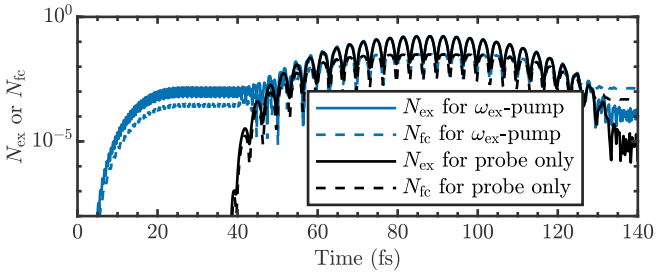

FIG. 12. Number of excitons N_{ex} and free carriers N_{fc} as a function of time, in blue for pump and probe, and in black for the probe-only case. Parameters of Fig. 11 are used, alongside a probe-only calculation.

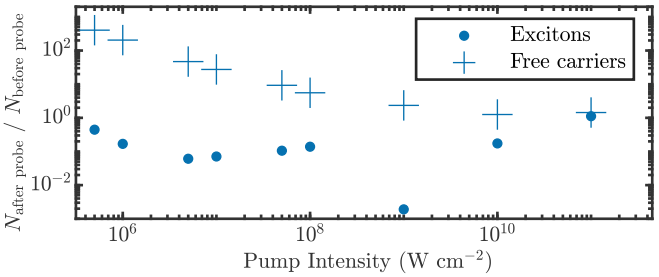

FIG. 13. Ratio of the number of excitons N_{ex} before and after the probe pulse (circles), and ratio of the number of free carriers N_{fc} before and after the probe pulse (crosses), as a function of pump intensity.

free carriers, during the probe pulse. Interestingly, our TDHF calculation predicts that seeding the sample with excitons is expected to be more efficient than seeding the sample with free carriers for above band-gap harmonic enhancement. This is despite of the fact, that here in Fig. 11, the degree of excitation in the free-carrier-seeded system is 2.3 times larger than the excitation of the exciton-seeded sample.

Utilizing the temporal dependency of the exciton wave function, we considered the temporal behavior of the number of excitons and free carriers during both the pump and probe processes, as shown in Fig. 12 for the exciton-seeded system. During the first 25 fs, the pump generates both excitons and free carriers. Hereafter, from 35 to 135 fs, the probe generates and dissociates excitons and generates free carriers. We note that the number of excitons and free carriers are generally gauge dependent during the interaction with an external electromagnetic field. Therefore, we only use these quantities for interpretation at field-free gauge-invariant time instances. From the pump-probe results, we conclude that the vast majority of the excitons generated by the pump are annihilated by the probe, as expected from an intense laser pulse. After the probe, the system has more free carriers than excitons, even if we started originally from mostly having a bound-exciton population. Comparing with the probe-only results, it appears that originally pumped excitons seem to contribute with an increase in the number of free carriers in the sample after the HHG process and an increased number of excitons. We therefore conclude that the presence of bound excitons in a sample can significantly change how the number of free carriers develops as a result of the HHG process. We performed this analysis for various pump intensities, as shown in Fig. 13. In the low-intensity regime, a large fraction of bound excitons generated by the pump are dissociated by the probe pulse to inject a significant contribution of free carriers. However, interesting, for higher pump intensity, for which a larger bound exciton population is prepared in the sample, the probe pulse injects less carriers, and dissociates less excitons (with a notable exception for 10^9 W cm^{-2}). This is another proof that the presence of bound excitons in the sample affects the probe-induced carrier dynamics, even in the strong-field regime. Importantly, we note that unlike what could be expected, having more excitons in the sample before the pump laser comes in does not lead to more excitons being dissociated, and for 10^{11} W cm^{-2}, we even end up with more bound excitons after the probe pulse than before, confirming the important role of the electron recombination pathway to generate bound excitons.

[1] R. Ulbricht, E. Hendry, J. Shan, T. F. Heinz, and M. Bonn, Rev. Mod. Phys. **83**, 543 (2011).

[2] S. Haastrup, S. Latini, K. Bolotin, and K. S. Thygesen, Phys. Rev. B **94**, 041401(R) (2016).

[3] C. J. Bardeen, Annu. Rev. Phys. Chem. **65**, 127 (2014).

[4] F. C. Spano, Annu. Rev. Phys. Chem. **57**, 217 (2006).

[5] P. Cudazzo, F. Sottile, A. Rubio, and M. Gatti, J. Phys.: Condens. Matter **27**, 113204 (2015).

[6] T. Mueller and E. Malic, npj 2D Mater. Applicat. **2**, 29 (2018).

[7] T. Unold, K. Mueller, C. Lienau, T. Elsaesser, and A. D. Wieck, Phys. Rev. Lett. **92**, 157401 (2004).

[8] T. H. Stievater, X. Li, D. G. Steel, D. Gammon, D. S. Katzer, D. Park, C. Piermarocchi, and L. J. Sham, Phys. Rev. Lett. **87**, 133603 (2001).

[9] U. Siegner, M. A. Mycek, S. Glutsch, and D. S. Chemla, Phys. Rev. Lett. **74**, 470 (1995).

[10] P. Merkl, F. Mooshammer, P. Steinleitner, A. Girnghuber, K.-Q. Lin, P. Nagler, J. Holler, C. Schüller, J. M. Lupton, T. Korn, S. Ovesen, S. Brem, E. Malic, and R. Huber, Nat. Mater. **18**, 691 (2019).

[11] G. Wang, A. Chernikov, M. M. Glazov, T. F. Heinz, X. Marie, T. Amand, and B. Urbaszek, Rev. Mod. Phys. **90**, 021001 (2018).

[12] Z. Qiu, M. Trushin, H. Fang, I. Verzhbitskiy, S. Gao, E. Laksono, M. Yang, P. Lyu, J. Li, J. Su *et al.*, Sci. Adv. **5**, eaaw2347 (2019).

[13] S. Manzeli, D. Ovchinnikov, D. Pasquier, O. V. Yazyev, and A. Kis, Nat. Rev. Mater. **2**, 17033 (2017).

[14] K. He, N. Kumar, L. Zhao, Z. Wang, K. F. Mak, H. Zhao, and J. Shan, Phys. Rev. Lett. **113**, 026803 (2014).

[15] P. Rivera, J. R. Schaibley, A. M. Jones, J. S. Ross, S. Wu, G. Aivazian, P. Klement, K. Seyler, G. Clark, N. J. Ghimire,

J. Yan, D. G. Mandrus, W. Yao, and X. Xu, Nat. Commun. **6**, 6242 (2015).
[16] H. Patel, R. W. Havener, L. Brown, Y. Liang, L. Yang, J. Park, and M. W. Graham, Nano Lett. **15**, 5932 (2015).
[17] K. Tran, G. Moody, F. Wu, X. Lu, J. Choi, K. Kim, A. Rai, D. A. Sanchez, J. Quan, A. Singh, J. Embley, A. Zepeda, M. Campbell, T. Autry, T. Taniguchi, K. Watanabe, N. Lu, S. K. Banerjee, K. L. Silverman, S. Kim *et al.*, Nature (London) **567**, 71 (2019).
[18] C. Trovatello, F. Katsch, N. J. Borys, M. Selig, K. Yao, R. Borrego-Varillas, F. Scotognella, I. Kriegel, A. Yan, A. Zettl *et al.*, Nat. Commun. **11**, 5277 (2020).
[19] E. A. Pogna, M. Marsili, D. De Fazio, S. Dal Conte, C. Manzoni, D. Sangalli, D. Yoon, A. Lombardo, A. C. Ferrari, A. Marini *et al.*, ACS Nano **10**, 1182 (2016).
[20] X. Jiang, Q. Zheng, Z. Lan, W. A. Saidi, X. Ren, and J. Zhao, Sci. Adv. **7**, eabf3759 (2021).
[21] E. Perfetto, Y. Pavlyukh, and G. Stefanucci, Phys. Rev. Lett. **128**, 016801 (2022).
[22] E. Perfetto and G. Stefanucci, Phys. Rev. B **103**, L241404 (2021).
[23] M. Massicotte, F. Vialla, P. Schmidt, M. B. Lundeberg, S. Latini, S. Haastrup, M. Danovich, D. Davydovskaya, K. Watanabe, T. Taniguchi *et al.*, Nat. Commun. **9**, 1633 (2018).
[24] G. Antonius and S. G. Louie, Phys. Rev. B **105**, 085111 (2022).
[25] D. Li, C. Trovatello, S. Dal Conte, M. Nuß, G. Soavi, G. Wang, A. C. Ferrari, G. Cerullo, and T. Brixner, Nat. Commun. **12**, 954 (2021).
[26] M. Lewenstein, P. Balcou, M. Y. Ivanov, A. L'Huillier, and P. B. Corkum, Phys. Rev. A **49**, 2117 (1994).
[27] S. Y. Kruchinin, F. Krausz, and V. S. Yakovlev, Rev. Mod. Phys. **90**, 021002 (2018).
[28] S. Shree, D. Lagarde, L. Lombez, C. Robert, A. Balocchi, K. Watanabe, T. Taniguchi, X. Marie, I. C. Gerber, M. M. Glazov, L. E. Golub, B. Urbaszek, and I. Paradisanos, Nat. Commun. **12**, 6894 (2021).
[29] F. Langer, M. Hohenleutner, C. P. Schmid, C. Poellmann, P. Nagler, T. Korn, C. Schüller, M. S. Sherwin, U. Huttner, J. T. Steiner, S. W. Koch, M. Kira, and R. Huber, Nature (London) **533**, 225 (2016).
[30] B. Zaks, R. B. Liu, and M. S. Sherwin, Nature (London) **483**, 580 (2012).
[31] J. Kono, M. Y. Su, T. Inoshita, T. Noda, M. S. Sherwin, S. J. Allen, Jr., and H. Sakaki, Phys. Rev. Lett. **79**, 1758 (1997).
[32] M. Lucchini, S. A. Sato, G. D. Lucarelli, B. Moio, G. Inzani, R. Borrego-Varillas, F. Frassetto, L. Poletto, H. Hübener, U. De Giovannini, A. Rubio, and M. Nisoli, Nat. Commun. **12**, 1021 (2021).
[33] R. Géneaux, C. J. Kaplan, L. Yue, A. D. Ross, J. E. Bækhøj, P. M. Kraus, H.-T. Chang, A. Guggenmos, M.-Y. Huang, M. Zürch, K. J. Schafer, D. M. Neumark, M. B. Gaarde, and S. R. Leone, Phys. Rev. Lett. **124**, 207401 (2020).
[34] A. Moulet, J. B. Bertrand, T. Klostermann, A. Guggenmos, N. Karpowicz, and E. Goulielmakis, Science **357**, 1134 (2017).
[35] Y. Kobayashi, C. Heide, A. C. Johnson, V. Tiwari, F. Liu, D. A. Reis, T. F. Heinz, and S. Ghimire, Nat. Phys. **19**, 171 (2023).
[36] M. Lein, N. Hay, R. Velotta, J. P. Marangos, and P. L. Knight, Phys. Rev. A **66**, 023805 (2002).
[37] R. Torres, N. Kajumba, J. G. Underwood, J. S. Robinson, S. Baker, J. W. G. Tisch, R. de Nalda, W. A. Bryan, R. Velotta, C. Altucci, I. C. E. Turcu, and J. P. Marangos, Phys. Rev. Lett. **98**, 203007 (2007).
[38] W. Li, X. Zhou, R. Lock, S. Patchkovskii, A. Stolow, H. C. Kapteyn, and M. M. Murnane, Science **322**, 1207 (2008).
[39] S. Baker, J. S. Robinson, C. A. Haworth, H. Teng, R. A. Smith, C. C. Chirilă, M. Lein, J. W. G. Tisch, and J. P. Marangos, Science **312**, 424 (2006).
[40] M. Lein, Phys. Rev. Lett. **94**, 053004 (2005).
[41] J. Itatani, J. Levesque, D. Zeidler, H. Niikura, H. Pépin, J. C. Kieffer, P. B. Corkum, and D. M. Villeneuve, Nature (London) **432**, 867 (2004).
[42] O. Schubert, M. Hohenleutner, F. Langer, B. Urbanek, C. Lange, U. Huttner, D. Golde, T. Meier, M. Kira, S. W. Koch, and R. Huber, Nat. Photonics **8**, 119 (2014).
[43] M. Garg, H. Y. Kim, and E. Goulielmakis, Nat. Photon. **12**, 291 (2018).
[44] G. Vampa, T. J. Hammond, N. Thiré, B. E. Schmidt, F. Légaré, C. R. McDonald, T. Brabec, D. D. Klug, and P. B. Corkum, Phys. Rev. Lett. **115**, 193603 (2015).
[45] S. Ghimire, A. D. DiChiara, E. Sistrunk, P. Agostini, L. F. DiMauro, and D. A. Reis, Nat. Phys. **7**, 138 (2011).
[46] T. T. Luu, M. Garg, S. Y. Kruchinin, A. Moulet, M. T. Hassan, and E. Goulielmakis, Nature (London) **521**, 498 (2015).
[47] N. Klemke, O. D. Mücke, A. Rubio, F. X. Kärtner, and N. Tancogne-Dejean, Phys. Rev. B **102**, 104308 (2020).
[48] C. Heide, Y. Kobayashi, A. C. Johnson, F. Liu, T. F. Heinz, D. A. Reis, and S. Ghimire, Optica **9**, 512 (2022).
[49] Y. S. You, D. Reis, and S. Ghimire, Nat. Phys. **13**, 345 (2017).
[50] K. Kaneshima, Y. Shinohara, K. Takeuchi, N. Ishii, K. Imasaka, T. Kaji, S. Ashihara, K. L. Ishikawa, and J. Itatani, Phys. Rev. Lett. **120**, 243903 (2018).
[51] A. A. Lanin, E. A. Stepanov, A. B. Fedotov, and A. M. Zheltikov, Optica **4**, 516 (2017).
[52] A. A. Lanin, E. A. Stepanov, A. V. Mitrofanov, D. A. Sidorov-Biryukov, A. B. Fedotov, and A. M. Zheltikov, Opt. Lett. **44**, 1888 (2019).
[53] T. T. Luu and H. J. Wörner, Nat. Commun. **9**, 916 (2018).
[54] O. Neufeld, N. Tancogne-Dejean, H. Hübener, U. De Giovannini, and A. Rubio, Phys. Rev. X **13**, 031011 (2023).
[55] G. Ndabashimiye, S. Ghimire, M. Wu, D. A. Browne, K. J. Schafer, M. B. Gaarde, and D. A. Reis, Nature (London) **534**, 520 (2016).
[56] H. Liu, Y. Li, Y. S. You, S. Ghimire, T. F. Heinz, and D. A. Reis, Nat. Phys. **13**, 262 (2017).
[57] M. Garg, M. Zhan, T. T. Luu, H. Lakhotia, T. Klostermann, A. Guggenmos, and E. Goulielmakis, Nature (London) **538**, 359 (2016).
[58] A. Trautmann, R. Zuo, G. Wang, W.-R. Hannes, S. Yang, L. H. Thong, C. Ngo, J. T. Steiner, M. Ciappina, M. Reichelt, H. T. Duc, X. Song, W. Yang, and T. Meier, in *Ultrafast Phenomena and Nanophotonics XXVI*, edited by M. Betz and A. Y. Elezzabi (International Society for Optics and Photonics - SPIE, Bellingham, WA, 2022), Vol. 11999, p. 1199909.
[59] J. Hader, J. Neuhaus, J. V. Moloney, and S. W. Koch, Opt. Lett. **48**, 2094 (2023).
[60] E. B. Molinero, B. Amorim, M. Malakhov, G. Cistaro, Álvaro Jiménez-Galán, M. Ivanov, A. Picón, P. San-José, and R. E. F. Silva, Formation, stability, and highly nonlinear optical

response of excitons to intense light fields interacting with two-dimensional materials, arXiv:2307.16647.
[61] K. Nagai, K. Uchida, S. Kusaba, T. Endo, Y. Miyata, and K. Tanaka, Phys. Rev. Res. **5**, 043130 (2023).
[62] M. Udono, K. Sugimoto, T. Kaneko, and Y. Ohta, Phys. Rev. B **105**, L241108 (2022).
[63] H. K. Avetissian, G. F. Mkrtchian, and K. Z. Hatsagortsyan, Phys. Rev. Res. **2**, 023072 (2020).
[64] H. K. Avetissian, S. S. Israelyan, H. H. Matevosyan, and G. F. Mkrtchian, Phys. Rev. A **105**, 063504 (2022).
[65] S. Beaulieu, S. Camp, D. Descamps, A. Comby, V. Wanie, S. Petit, F. Légaré, K. J. Schafer, M. B. Gaarde, F. Catoire, and Y. Mairesse, Phys. Rev. Lett. **117**, 203001 (2016).
[66] A. Picón, L. Roso, J. Mompart, O. Varela, V. Ahufinger, R. Corbalán, and L. Plaja, Phys. Rev. A **81**, 033420 (2010).
[67] C. Yu, K. K. Hansen, and L. B. Madsen, Phys. Rev. A **99**, 013435 (2019).
[68] S. Schmitt-Rink, D. S. Chemla, and H. Haug, Phys. Rev. B **37**, 941 (1988).
[69] G. Stefanucci and R. Van Leeuwen, *Nonequilibrium Many-body Theory of Quantum Systems: A Modern Introduction* (Cambridge University Press, Cambridge, 2013).
[70] K. Balzer and M. Bonitz, *Nonequilibrium Green's Functions Approach to Inhomogeneous Systems* (Springer, Berlin, 2012).
[71] P. Lipavský, V. Špička, and B. Velický, Phys. Rev. B **34**, 6933 (1986).
[72] Y. Pavlyukh, E. Perfetto, D. Karlsson, R. van Leeuwen, and G. Stefanucci, Phys. Rev. B **105**, 125134 (2022).
[73] W. Hanke and L. J. Sham, Phys. Rev. Lett. **33**, 582 (1974).
[74] Y.-H. Kim and A. Görling, Phys. Rev. Lett. **89**, 096402 (2002).
[75] J. Sun, C.-W. Lee, A. Kononov, A. Schleife, and C. A. Ullrich, Phys. Rev. Lett. **127**, 077401 (2021).
[76] J. Sun, J. Yang, and C. A. Ullrich, Phys. Rev. Res. **2**, 013091 (2020).
[77] J. R. Williams, N. Tancogne-Dejean, and C. A. Ullrich, J. Chem. Theory Comput. **17**, 1795 (2021).
[78] T. Ikemachi, Y. Shinohara, T. Sato, J. Yumoto, M. Kuwata-Gonokami, and K. L. Ishikawa, Phys. Rev. A **98**, 023415 (2018).
[79] N. Tancogne-Dejean, M. J. T. Oliveira, X. Andrade, H. Appel, C. H. Borca, G. Le Breton, F. Buchholz, A. Castro, S. Corni, A. A. Correa, U. De Giovannini, A. Delgado, F. G. Eich, J. Flick, G. Gil, A. Gomez, N. Helbig, H. Hübener, R. Jestädt, J. Jornet-Somoza *et al.*, J. Chem. Phys. **152**, 124119 (2020).
[80] L. Lin, J. Chem. Theory Comput. **12**, 2242 (2016).
[81] P. Carrier, S. Rohra, and A. Görling, Phys. Rev. B **75**, 205126 (2007).
[82] G. F. Bertsch, J.-I. Iwata, A. Rubio, and K. Yabana, Phys. Rev. B **62**, 7998 (2000).
[83] S. A. Mewes, J.-M. Mewes, A. Dreuw, and F. Plasser, Phys. Chem. Chem. Phys. **18**, 2548 (2016).
[84] Y. Li and C. Ullrich, Chem. Phys. **391**, 157 (2011).
[85] M. K. Man, J. Madéo, C. Sahoo, K. Xie, M. Campbell, V. Pareek, A. Karmakar, E. L. Wong, A. Al-Mahboob, N. S. Chan *et al.*, Sci. Adv. **7**, eabg0192 (2021).
[86] S. Dong, M. Puppin, T. Pincelli, S. Beaulieu, D. Christiansen, H. Hübener, C. W. Nicholson, R. P. Xian, M. Dendzik, Y. Deng *et al.*, Nat. Sci. **1**, e10010 (2021).
[87] M. S. Prete, D. Grassano, O. Pulci, I. Kupchak, V. Olevano, and F. Bechstedt, Sci. Rep. **10**, 10719 (2020).
[88] P. Stampfli and K. H. Bennemann, Phys. Rev. B **46**, 10686 (1992).
[89] P. Stampfli and K. H. Bennemann, Phys. Rev. B **49**, 7299 (1994).
[90] P. Stampfli and K. H. Bennemann, Phys. Rev. B **42**, 7163 (1990).
[91] P. D. Keathley, S. V. B. Jensen, M. Yeung, M. R. Bionta, and L. B. Madsen, Phys. Rev. B **107**, 054302 (2023).
[92] G. Vampa, C. R. McDonald, G. Orlando, P. B. Corkum, and T. Brabec, Phys. Rev. B **91**, 064302 (2015).
[93] C. Yu, H. Iravani, and L. B. Madsen, Phys. Rev. A **102**, 033105 (2020).
[94] C.-M. Wang, N. Tancogne-Dejean, M. Altarelli, A. Rubio, and S. A. Sato, Phys. Rev. Res. **2**, 033333 (2020).
[95] L. Yue and M. B. Gaarde, Phys. Rev. Lett. **124**, 153204 (2020).
[96] T. Ikemachi, Y. Shinohara, T. Sato, J. Yumoto, M. Kuwata-Gonokami, and K. L. Ishikawa, Phys. Rev. A **95**, 043416 (2017).
[97] N. Tancogne-Dejean, O. D. Mücke, F. X. Kärtner, and A. Rubio, Phys. Rev. Lett. **118**, 087403 (2017).
[98] M. Kira and S. W. Koch, *Semiconductor Quantum Optics* (Cambridge University Press, Cambridge, 2011).
[99] T. Ogawa and T. Takagahara, Phys. Rev. B **43**, 14325 (1991).
[100] T. Ogawa and T. Takagahara, Phys. Rev. B **44**, 8138 (1991).
[101] U. De Giovannini, A. H. Larsen, and A. Rubio, Eur. Phys. J. B **88**, 56 (2015).